Acoustic emission source localization and velocity determination of the fundamental mode A_0 using wavelet analysis and a Newton-based optimization technique

F. Ciampa, M.Meo
Material Research Centre, Department of Mechanical Engineering,
University of Bath, Bath, UK

Abstract

This paper investigates the development of an *in-situ* impact detection monitoring system able to identify in real-time the acoustic emission location. The proposed algorithm is based on the differences of stress waves measured by surface bonded piezoelectric transducers. A joint time frequency analysis based on the magnitude of the Continuous Wavelet Transform was used to determine the time of arrivals of the wave packets. A combination of unconstrained optimization technique associated to a local Newton's iterative method was employed to solve a set of non linear equations in order to assess the impact location coordinates and the wave speed. With the proposed approach, the drawbacks of a triangulation method in terms to estimate *a priori* the group velocity and the need to find the best time-frequency technique for the time of arrival determination were overcome. Moreover, this algorithm proved to be very robust since it was able to converge from almost any guess point and required little computational time. A comparison between the theoretical and experimental results carried out with piezoelectric film (PVDF) and acoustic emission transducers showed that the impact source location and the wave velocity were predicted with reasonable accuracy. In particular, the maximum error in estimation of the impact location was less than 2% and about 1% for the flexural waves velocity.

Keywords: Impact location identification, Continuous Wavelet Transform, PVDF, flexural waves.

1 Introduction and statement of the problem

A real-time knowledge of the impact location source is fundamental in both Non-Destructive Evaluation (NDE) techniques as well as Structural Health Monitoring (SHM) systems. The ability to locate the impact response can be achieved through *passive technique*, wherein the signals emitted by internal or external sources are measured by ultrasonic transducers directly on the specimen surface or embedded into the structure (Balageas et al., 2006).

Most of these techniques deal with the detection of Lamb waves caused by low velocity impacts. According to Viktorov (1967) theory, Lamb waves are stress waves that propagate within thin solid plates with free boundaries. Depending on the product of frequency times thickness, an infinite number of modes for both *symmetric* and *antisymmetric* displacements are available. Symmetric modes (S_n) are related to the

extensional modes as displacements occur in the direction of wave propagation, whilst antisymmetric modes (A_n) are known as flexural modes as the displacements pattern is transverse to the plane of the plate. These Lamb modes differ in their phase and group velocities as well as in the strain and stress field.

Estimating the location of an AE source is an inverse problem based on the detection of the time at which the stressed wave reaches a number of sensors. Several studies presents in literature were focused on the *in situ* investigations of Lamb waves using piezoelectric transducers attached to plate-like structures (El youbi et al., 2004; Giurgiutiu, 2002). An alternative to these conventional transducers was the employment of polyvinyldilene fluoride (PVDF) film sensors for AE applications (Hamstad M A, 1995; Brown et al., 1996; Gaul and Hurlebaus, 1999; Monkhouse et al., 2000). These smart materials bonded on the surface of the structures own the characteristic of better interrogate large areas with a low cost availability, easily handle and broad-band acoustic performance.

Usually, most of the methods for impact location use the triangulation technique (also known as Tobias algorithm), wherein the impact point is identified as the intersection of three circles, whose centres are the sensors location (Tobias, 1976). This approach is strongly limited by the assumption that wave velocity must be known and remains the same in all directions, but this is not true especially in anisotropic and inhomogeneous materials. Moreover, the flexural wave velocity is not constant, but it is function of the signal frequency that depends on the impact speed of the object hitting the structure.

Furthermore, due to the dispersive nature of the flexural modes or to the uncertainty of the noise level of the signal measured, a suitable choice of the time–frequency analysis for the identification of the time of arrival (TOA) is necessary. In these terms, Ziola and Gorman (1991) employed a cross-correlation technique for determining the time of propagation, whilst Kosel et al. (2003) used a combination of cross-correlation function with an appropriate bandpass-filter. In both approaches the maximum of the cross-correlation coefficient of two signals indicates the delay time between them. However, these methods present such limits especially when the sensors are placed close to the edges. In fact, multiple reflections from the boundaries generate ambiguous peaks in cross-correlation coefficients causing poor localisation results. Seydel and Chang (2001) proposed an approach based on a double peak method wherein the arrival time was chosen by selecting the minimum before the maximum for each signal. Nevertheless, the dependence of the wave velocity on frequency and the ambiguity of the noise level make this method inappropriate for the purpose of correct determination of the impact source. Therefore the use of the Continuous Wavelet Transform (CWT) that provides high resolution for a wide range of frequencies was found to guarantee more accuracy in the time-frequency analysis of acoustic waves (e.g. Meo et al., 2005; Jeong and Jung, 2000).

Real-time impact algorithms must exhibit the best tradeoffs in terms of *efficiency* and *accuracy* and must require very little computational time (CPU cost) for different use in a SHM system. Kundu et al. (2009) developed an optimization algorithm for the determination of point of impact on aluminium and composite structures, based on minimizing an error function that used the difference of TOA of AE signals. Gaul et al. (2001) applied a Gauss-Newton method to non linear least square optimization to analyze “synthetic” AE signals. Conversely, an alternative approach to model-based

methods for the identification of the impact location was the artificial neural network approach (Sung et al., 2000). Despite this method is suitable for complex structure, it cannot provide an optimum solution.

The research study conducted in this paper was aimed to overcome the limits of a triangulation method for a real-time localization of the impact source and to exhibit the best approach for the time of arrival determination. In fact, the present work reports the creation of an algorithm for *in-situ* impact detection (AE) and wave velocity identification in isotropic structures, using a network of piezoelectric transducers. To assess the impact location and the wave velocity, the basic idea was to combine a globally convergent strategy, based on an *unconstrained optimization* associated to a local Newton-Raphson iterative method. In addition, the information contained in the time-frequency graph of the magnitude of the Continuous Wavelet Transform was used to determine the time of propagation of the stress waves. To validate the method, two different experiments with piezoelectric-film (PVDF) and Acoustic Emission sensors were carried out. Figure 1 illustrates the architecture of the impact location and wave velocity determination system.

The layout of the paper is as follow: in Section 2 the algorithm for the source location and wave velocity evaluation algorithm is presented. Section 3 outlines the main characteristics of the Continuous Wavelet Transform in terms of multi-resolution analysis and energy density of the signal for the time of arrival identification. In Section 4 the local Newton's iterative method associated to an *unconstrained optimization* for solving systems of non-linear equations is described. Section 5 reports the experimental set-up and the analysis results. Then, the final conclusions of the method adopted are discussed.

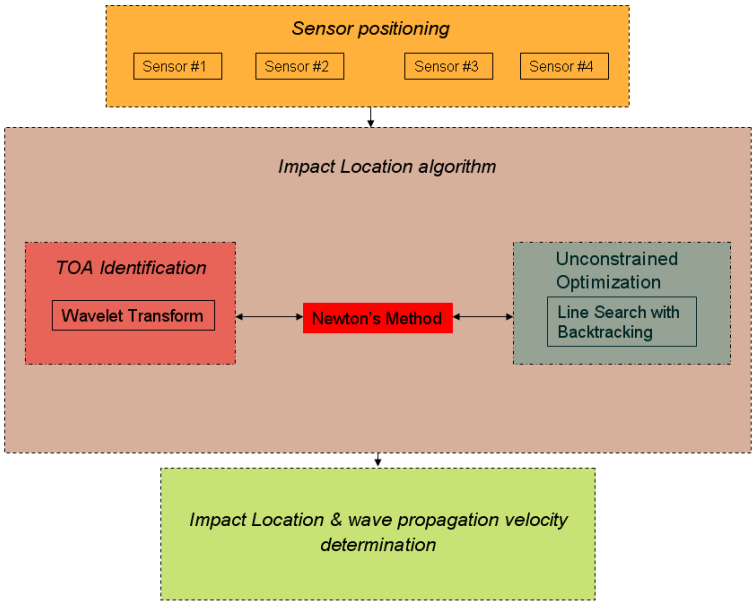

Figure 1 Architecture of impacts source location and wave velocity identification system

2 Impact location and group wave velocity algorithm

The algorithm for the impact source location and wave velocity determination is based on the differences of acoustic emission (AE) signals measured by four piezoelectric transducers attached on the surface of an aluminium structure. As the medium of interest is isotropic and homogeneous, from classical theory of thin elastic plate (Reddy, 1999), the extensional wave group velocity $c_l(\omega)=\sqrt{\frac{E}{\rho(1-\nu)^2}}$ and the flexural wave velocity $c_f(\omega)=\left[\frac{Eh^2}{12\rho(1-\nu^2)}\omega^2\right]^{1/4}$ are related by only density ρ, thickness h, angular frequency ω, Young modulus E and Poisson ratio ν. Hence, in this algorithm, the group velocity can be considered independent of propagation direction.

The origin of the Cartesian reference frame was arranged at the left bottom corner of the plate. The impact source point I is at unknown coordinates (x_I, y_I) in the plane of the plate and the sensors are located at distance d_i $(i=1,\ldots,4)$ from the source (Fig. 2). Furthermore, the dimensions of the plate are L, length and W, width.

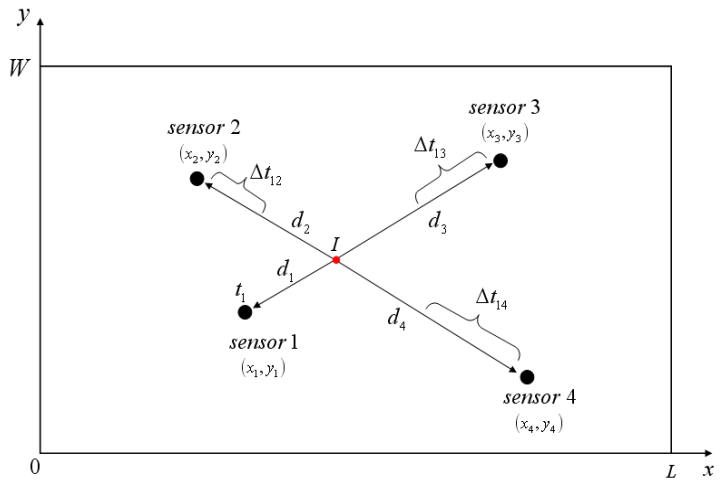

Figure 2 Impact location and wave velocity identification procedure

The resulting system of equation for the source location problem and wave speed identification is given as follow:

$$d_i=\sqrt{(x_i-x_I)^2+(y_i-y_I)^2} \quad (2.1)$$

$$t_i=\frac{d_i}{V_g} \quad (2.2)$$

where V_g is the velocity of propagation of the stressed wave, t_i is the time of detection of the AE signals and (x_i, y_i) are the coordinates of the i-th sensor. Combining equations (2.1) and (2.2) we obtain:

$$(x_i-x_I)^2+(y_i-y_I)^2-(t_i\cdot V_g)^2=0 \quad (2.3)$$

which is the equation of circumference with radius $r^2 = (t_i \cdot V_g)^2$. Equation (2.3) can be expanded into the following set of equations, with the unknown t_i, x_I, y_I and V_g:

$$\begin{cases} (x_1 - x_I)^2 + (y_1 - y_I)^2 - (t_1 \cdot V_g)^2 = 0 \\ (x_2 - x_I)^2 + (y_2 - y_I)^2 - (t_2 \cdot V_g)^2 = 0 \\ (x_3 - x_I)^2 + (y_3 - y_I)^2 - (t_3 \cdot V_g)^2 = 0 \\ (x_4 - x_I)^2 + (y_4 - y_I)^2 - (t_4 \cdot V_g)^2 = 0 \end{cases} \quad (2.4)$$

This is a system of four equations with seven unknown. If t_1 is the travel time required to reach the sensor 1 (*master sensor*) and Δt_{1j} $(j = 2,3,4)$ are the time difference between the sensor 1 and the other sensors, we can write:

$$\begin{cases} t_2 = t_1 \pm \Delta t_{12} \\ t_3 = t_1 \pm \Delta t_{13} \\ t_4 = t_1 \pm \Delta t_{14} \end{cases} \quad (2.5)$$

and system (2.4) becomes:

$$\begin{cases} (x_1 - x_I)^2 + (y_1 - y_I)^2 - (t_1 V_g)^2 = 0 \\ (x_2 - x_I)^2 + (y_2 - y_I)^2 - [(t_1 + \Delta t_{12}) \cdot V_g]^2 = 0 \\ (x_3 - x_I)^2 + (y_3 - y_I)^2 - [(t_1 + \Delta t_{13}) \cdot V_g]^2 = 0 \\ (x_4 - x_I)^2 + (y_4 - y_I)^2 - [(t_1 + \Delta t_{14}) \cdot V_g]^2 = 0 \end{cases} \quad (2.6)$$

Location and wave velocity must be calculated by solving this set of non linear equations with the unknown $\mathbf{x} = (x_I, y_I, t_1, V_g)$. The three time differences Δt_{1j} must be determined through an appropriate time-frequency analysis.

Next Section outlines the characteristics of the Continuous Wavelet Transform for the time of wave propagation identification, whilst Section 3 describes the algorithm aimed to solve the set of non linear equations (2.6) for the assessment of the impact location coordinates and the speed of Lamb wave A_0.

3 The Continuous Wavelet Transform

Due the dependence of the wave velocity on frequency and the ambiguity of the noise level, a good impact detection method necessitates of a suitable choice of the time–frequency analysis for the time arrival identification.

Wavelet transformation method provides a good compromise between location and frequency resolution and it is able to analyze low and high frequencies at the same time, even respecting the *uncertainty principle* (also known as *Heisenberg inequality*). Let $\psi \in L^1(\Re) \cap L^2(\Re)$ be the analysing wavelet called also the *mother wavelet*, where

$\Re$ is the domain of real numbers and the space $L^2(\Re)$ is the set of all square-integrable functions defined on $\Re$. The mother wavelet must satisfy the *admissibility condition* defined as:

$$\int_{-\infty}^{+\infty} \frac{|\hat{\psi}(\omega)|^2}{|\omega|} d\omega < \infty \qquad (3.1)$$

where $\hat{\psi}$ is the Fourier transform of ψ. Eq. (3.1) is the necessary condition for ensuring the existence of the inverse wavelet transform. The Continuous Wavelet Transform (CWT) is a linear transform that decomposes an arbitrary signal $f(t)$ through basis functions that are simply dilatations and translations of a parent wavelet $\psi(t)$, by the continuous convolution of the signal and the scaled or shifted wavelet (Mallat, 1998):

$$WT(a,b) = \left\langle f(t) \middle| \psi_{a,b}(t) \right\rangle = \frac{1}{\sqrt{a}} \int_{-\infty}^{+\infty} f(t) \psi^* \left(\frac{t-b}{a} \right) dt \quad (3.2)$$

where $\psi^*(t)$ denotes the complex conjugate of the mother wavelet $\psi(t)$, a is the dilatation or scale parameter defining the support width of the wavelet and b the translation parameter localising the wavelet in the time domain. The factor $1/\sqrt{a}$ is used to ensure that all wavelets at all scales have the same area and contain the same energy.

The time-frequency resolution of the wavelet transform can be expressed as function of the scale parameter *a* through the following relationships:

$$\begin{aligned} \Delta t &= a^m \Delta t_\psi \\ \Delta \omega &= a^{-m} \Delta \omega_\psi \end{aligned} \qquad (3.3)$$

where Δt_ψ and $\Delta \omega_\psi$ are the duration and bandwidth of the wavelet function, respectively, and $m \in Z$ with *Z* the set of positive integers.

According to the uncertainty principle (Le and Argoul, 2004), time-frequency localization domain for any time frequency point is a rectangle of width $a^m \Delta t$ and height $a^{-m} \Delta \omega$ with a constant area of $\Delta t \Delta f$. Consequently, time resolution of the CWT increases as frequency decreases and frequency resolution increases as time decreases. For these reasons, differently from the Short Time Fourier Transform wherein resolution is constant, the CWT is called *multi-resolution analysis*.

3.1 Morlet wavelet

Several studies present in literature deal with the use of the wavelet transform applied to acoustic emission (Hamstad et al., 2002). Gaul and Hurlebaus (1999) and Jeong and Jung (2000) applied the Gabor wavelet to identify the coordinates of an impact load on aluminium plate and Meo et al. (2005) used the Morlet wavelet to detect a source location of an acoustic emission on CFRP composite panel. In this study complex Morlet wavelet was employed as, in contrast with real wavelets, is able to separate amplitude and phase, enabling the measurement of instantaneous frequencies and their temporal evolution (Mallat S., 1998). Furthermore, it was experienced (Meo et

al., 2005) that Morlet wavelet enables the measurement of the localization frequency for signals with faster and slower oscillations, providing a flexible window that narrows at high frequencies and widens when observing low-frequency phenomena. The complex Morlet wavelet is expressed by the following equation:

$$\psi(t) = \frac{1}{\sqrt{\pi F_b}} e^{j\omega_c t} e^{-\frac{t^2}{F_b}} = \frac{1}{\sqrt{\pi F_b}} e^{-\frac{t^2}{F_b}} \left[\cos(\omega_c t) + j\sin(\omega_c t)\right] \qquad (3.4)$$

Morlet wavelet seems like an impulsive waveform with a *central frequency* $f_c = \omega_c / 2\pi$ when its *shape control parameter* F_b (wavelet bandwidth) can be set to be a small value. Conversely, when F_b increases, the wavelet waveform tends to be a harmonic waveform (Fig. 3). However, for practical purposes, because of the fast decay of its envelope towards zero, Morlet wavelet is considered admissible for $\omega_c \geq 5$. Furthermore, maximising equation (3.4) in the frequency domain, we obtain a unique relation between the scale parameter *a* and frequency of interest *f:*

$$f = \frac{f_c}{a} \qquad (3.5)$$

$$\hat{\psi}(af) = e^{-\pi^2 F_b (af - f_c)^2} \qquad (3.6)$$

where $\hat{\psi}(af)$ is the Fourier transform of $\psi(t)$.

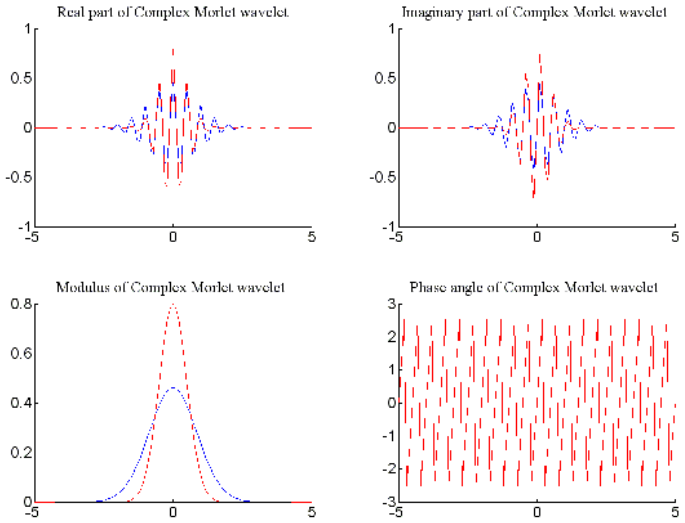

Figure 3 (a) (b) (c) (d) Morlet wavelet with different values of Fb (1.5 blue colour, 0.1 red colour). In figures (a) and (b) are represented the real and imaginary part of Morlet wavelet, whilst figures (c) and (d) depict the modulus and the phase angle.

3.2 Time of arrival identification using the CWT

CWT coefficients are useful for the identification of non stationary signals like transient phenomena hidden in vibration signals or impacts (Kim and Melheim, 2004).

In particular, the real part of the CWT is well suited for the determination of dominant scales, whilst the squared modulus of the CWT called also *scalogram* indicates the energy density of the signal at each scale at any time (Mallat S., 1998).

Hence, the scalogram is able to reveal the highest local energy content of the waveform measured. The squared modulus can be express as:

$$\left|WT(a,b)\right|^2 = WT(a,b)\cdot WT^*(a,b) \qquad (3.7)$$

Furthermore, the maximum value of the coefficients of the scalogram with a high concentration of energy is achieved at the *instantaneous frequency*, corresponding to the dominant frequency in the signal analysed at each instant in time. These coefficients taken at the instantaneous frequency in a time-frequency domain determine the *ridges* (Mallat S., 1998; Haase and Widjajakusuma, 2003). Therefore, the frequency of interest is chosen as the dominant frequency in the signal analysed by each sensor at each instant in time, i.e. the frequency corresponding at the maximum value of the Continuous Wavelet Transform squared modulus coefficients (ridges). Each frequency of interest is related to the scale parameter by the following relationship:

$$freq = \frac{f_c}{aT} \qquad (3.8)$$

where $freq$ is the frequency of interest, f_c is the central frequency of the wavelet used and T is the sampling period. The projection on the time domain of the ridge corresponds to the time of arrival (TOA) of the stress waves (Fig. 4). Once the TOA is known, we can calculate the time differences Δt_{1j} (eq. 2.5) with respect to the master sensor. Hence, based on the algorithm discussed in the next Section, the coordinates of the impact source location and wave group velocity can be determined.

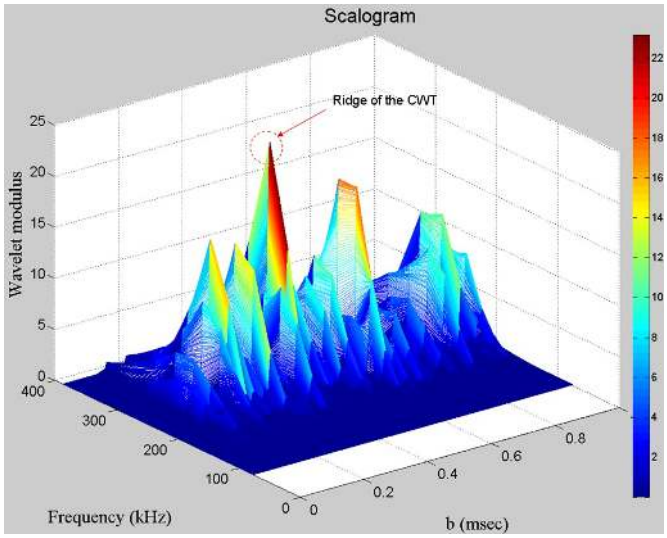

Figure 4 3-D plot of the scalogram of the CWT in which the ridge is took at the instantaneous frequency of 310 kHz

4 Newton's method for solving systems of non-linear equations

The strategy adopted in this paper to solve the set of equations (2.6) and to make the algorithm robust and convergent from almost any guess point is to combine a Newton's method with a Line Search algorithm.

Newton-Raphson or Newton's method is a very efficient iterative algorithm for finding the roots of non linear system of equations, since it locally converges from around an initial guess point $\mathbf{x}_0$ sufficiently close to the root (Dennis, 1996).

Let assume $F_i : \Re^n \to \Re^n$, where $\Re^n$ denotes n-dimensional Euclidean space, to be a twice *Lipschitz continuously* differentiable function. The set of non linear equations (2.6) can be expressed as:

$$\mathbf{F}(\mathbf{x}) = 0 \qquad (4.1)$$

where $\mathbf{F}$ is the vector of the functions F_i $(i = 1,\ldots,4)$ and $\mathbf{x}$ is the vector of unknown x_j $(j = 1,\ldots,4)$. Equation (4.1) has a zero at $\mathbf{x}^* \in \Re^n$ such that $\mathbf{F}(\mathbf{x}^*) = 0$.

Newton's method converges quadratically to $\mathbf{x}^*$ (i.e. the order of convergence is approximately two) by computing the Jacobian linearization of the function $\mathbf{F}$ around a guess point $\mathbf{x}_0$, and then using this linearization to move closer to the desired zero. The Newton iterate $\mathbf{x}^{n+1}$ from a current point $\mathbf{x}^n$ is given by:

$$\mathbf{x}^{n+1} = \mathbf{x}^n + \delta\mathbf{x}^n = \mathbf{x}^n - \mathbf{J}(\mathbf{x}^n)^{-1} \cdot \mathbf{F}(\mathbf{x}^n) \qquad (4.2)$$

where $\delta\mathbf{x} = \left[-\mathbf{J}(\mathbf{x})^{-1} \cdot \mathbf{F}(\mathbf{x})\right]$ is the Newton step and $\mathbf{J}(\mathbf{x})$ is the Jacobian matrix, which contains first derivatives of the objective function $\mathbf{F}(\mathbf{x})$ with respect to the four unknowns of the problem:

$$\mathbf{J}(\mathbf{x}) = \frac{\partial \mathbf{F}(\mathbf{x})}{\partial \mathbf{x}} = \begin{bmatrix} \frac{\partial F_1(\mathbf{x})}{\partial x_I} & \frac{\partial F_1(\mathbf{x})}{\partial y_I} & \frac{\partial F_1(\mathbf{x})}{\partial t_1} & \frac{\partial F_1(\mathbf{x})}{\partial V_g} \\ \frac{\partial F_2(\mathbf{x})}{\partial x_I} & \frac{\partial F_2(\mathbf{x})}{\partial y_I} & \frac{\partial F_2(\mathbf{x})}{\partial t_1} & \frac{\partial F_2(\mathbf{x})}{\partial V_g} \\ \frac{\partial F_3(\mathbf{x})}{\partial x_I} & \frac{\partial F_3(\mathbf{x})}{\partial y_I} & \frac{\partial F_3(\mathbf{x})}{\partial t_1} & \frac{\partial F_3(\mathbf{x})}{\partial V_g} \\ \frac{\partial F_4(\mathbf{x})}{\partial x_I} & \frac{\partial F_4(\mathbf{x})}{\partial y_I} & \frac{\partial F_4(\mathbf{x})}{\partial t_1} & \frac{\partial F_4(\mathbf{x})}{\partial V_g} \end{bmatrix} \qquad (4.3)$$

Newton's method can be modified and enhanced in various ways for solving systems of non linear equations, but in particular conditions, when the starting point is not near the root, it may not converge (Nocedal, 1999). The reasons for this failure are that the direction of the current iterate $\mathbf{x}^n$ may differ to be a direction of descent for $\mathbf{F}$, and, even if a search direction is a direction of decrease of $\mathbf{F}$, the length of the Newton step $\delta\mathbf{x}$ may be too long. Hence, a globally convergent algorithm associated to a Newton's method can be designed to find the solution of a system of non linear equations from almost any guess point $\mathbf{x}_0$. The approach adopted in this paper was to combine the Newton's method applied to the system (2.6) with the unconstrained problem of minimizing the *objective function* $\mathbf{F}$:

$$\min_{x \in \Re^n} \mathbf{F} : \Re^n \to \Re \qquad (4.4)$$

In unconstrained optimization, the most widely used function to be minimized (also known as *merit function*) is a scalar-valued function of $\mathbf{F}$, i.e. the squared norm of $\mathbf{F}$:

$$f(\mathbf{x}) = \frac{1}{2}\|\mathbf{F}(\mathbf{x})\|^2 = \frac{1}{2}\mathbf{F}(\mathbf{x})\cdot\mathbf{F}(\mathbf{x}) \qquad (4.5)$$

where the factor $\frac{1}{2}$ is introduced for convenience. Obviously any root of f fulfils the identity $f(\mathbf{x}^*) = 0$. Among the class of powerful algorithms for unconstrained optimization, in this paper we will focus on the Line-Search methods because of its simplicity, and because they do not depend on how the Jacobian is obtained. Furthermore, if the initial Newton step is proved to be unsatisfactory, the polynomial backtracking method will be considered.

4.1 Line Search methods with step selection by backtracking

In Line Search method the algorithm chooses a direction $\delta\mathbf{x}^n$ and searches along this direction from the current iterate to a new iterate $\mathbf{x}^{n+1}$ that guarantees a lower value of $f(\mathbf{x})$. The iteration is expressed by the following formula:

$$\mathbf{x}^{n+1} = \mathbf{x}^n + \lambda^n\delta\mathbf{x}^n \qquad 0 < \lambda \le 1 \qquad (4.6)$$

where λ is called *step length*. Whether the initial iterate $\mathbf{x}_0$ is close to the solution, the common strategy is to use a full Newton step $\delta\mathbf{x}^n$ by setting $\lambda = 1$. Otherwise, we move downhill along the Newton direction trying a sufficiently small value of λ until $\mathbf{x}^{n+1}$ satisfies the following criterion (known as *Armijo condition*):

$$f(\mathbf{x}^n + \lambda^n\delta\mathbf{x}^n) \le f(\mathbf{x}^n) + \alpha\,\lambda^n\nabla f(\mathbf{x}^n)^T\cdot\delta\mathbf{x}^n \qquad (4.7)$$

A good value of the parameter α is 10^{-4}. The *descent direction* of the Newton step from the current point $\mathbf{x}^n$ to a new point $\mathbf{x}^{n+1}$ is verified by the fact that the directional derivative of f at $\mathbf{x}^n$ in the direction $\delta\mathbf{x}^n$ is negative:

$$\begin{aligned}\nabla f(\mathbf{x}^n)\cdot\delta\mathbf{x}^n &= \frac{1}{2}\nabla\left[\mathbf{F}(\mathbf{x}^n)\cdot\mathbf{F}(\mathbf{x}^n)\right]\cdot\delta\mathbf{x}^n = \\ &= \left[\mathbf{F}(\mathbf{x}^n)\cdot\mathbf{J}(\mathbf{x}^n)\right]\cdot\left[-\mathbf{J}^{-1}(\mathbf{x}^n)\cdot\mathbf{F}(\mathbf{x}^n)\right] = -\mathbf{F}(\mathbf{x}^n)\cdot\mathbf{F}(\mathbf{x}^n) < 0\end{aligned} \qquad (4.8)$$

Moreover, the strategy for reducing λ guarantees that the Newton step may not be too large. The procedure can be performed through a backtracking Line-Search method (Dennis, 1996). It consists in finding the value of λ which minimizes the model of the following polynomial function:

$$g(\lambda^n) = f(\mathbf{x}^n + \lambda^n\delta\mathbf{x}^n) \qquad (4.9)$$

Hence, given any descent direction $\delta\mathbf{x}^n$, equation (4.9) satisfies (4.7) and (4.8) such that:

$$g'(\lambda^n) = \nabla f(\mathbf{x}^n)^T\cdot\delta\mathbf{x}^n \qquad (4.10)$$

Initially, the model of g is given and assumed linear:

$$\begin{cases} g(0) = f(\mathbf{x}^n) \\ g'(0) = \nabla f(\mathbf{x}^n)^T \cdot \delta\mathbf{x}^n \end{cases} \quad (4.11)$$

Setting $\lambda_0 = 1$, if the model satisfies the following condition:

$$g(1) > g(0) + \alpha\, g'(0) \quad (4.12)$$

we terminate the search. Otherwise, $g(\lambda)$ is expressed through a quadratic approximation by interpolating the three information available, $g(0)$, $g(1)$ and $g'(0)$:

$$g_q(\lambda) \approx [g(1) - g(0) - g'(0)]\lambda^2 + g'(0)\lambda + g(0) \quad (4.13)$$

The new trial value λ_1 is defined as the minimiser of $g_q(\lambda)$:

$$\lambda_1 = -\frac{g'(0)\lambda_0^2}{2[g(1) - g(0) - g'(0)]} \quad (4.14)$$

If λ_1 is too small the quadratic model is poorly accurate and we set a limit value of λ, $\lambda_{\min} = 0.1$. Conversely, a cubic model of $g_c(\lambda)$ is more acceptable since it provides more accuracy especially in situations where f has a negative curvature:

$$g_c(\lambda) = a\lambda^3 + b\lambda^2 + g'(0)\lambda + g(0) \quad (4.15)$$

From eq. (4.15), solving with respect to the coefficients a and b, we obtain a set of two equations using the last two previous values of λ ($g(\lambda_0)$ and $g(\lambda_1)$):

$$\begin{bmatrix} a \\ b \end{bmatrix} = \frac{1}{\lambda_0^2\lambda_1^2(\lambda_1 - \lambda_0)} \begin{bmatrix} \lambda_0^2 & -\lambda_1^2 \\ -\lambda_0^3 & \lambda_1^3 \end{bmatrix} \begin{bmatrix} g(\lambda_1) - g(0) - g'(0)\lambda_1 \\ g(\lambda_2) - g(0) - g'(0)\lambda_2 \end{bmatrix} \quad (4.16)$$

By differentiating eq. (4.13), the minimum point λ_2 is given by:

$$\lambda_2 = \frac{-b + \sqrt{b^2 - 3ag'(0)}}{3a} \quad (4.17)$$

Therefore, if any λ_i is either too close and smaller than λ_{i-1}, λ_i must be limited between the values $\lambda_{\max} = 0.5\lambda_{i-1}$ and $\lambda_{\min} = 0.1\lambda_i$. This procedure allows obtaining reasonable progress on each iteration, and the final λ will not be too small.

Thereby, with this procedure the algorithm was optimized and using the code written in Matlab on a standard pc, the computational time for each source location was less than 2 s, which means that the results can be obtained in quasi real-time using a compiled code.

5 Experimental set-up and procedure

Two different experiments were carried out for the validation tests in the present study. In test 1, an aluminium plate with dimensions 520 mm x 410 mm x 0.97 mm was

employed with four commercially available piezoelectric-film (PVDF) sensors (thickness 110 μm, length 420 mm) adhesively surface bonded (Fig. 8). These smart materials bonded on the surface of the structure own the characteristic of better interrogate large areas with a low cost availability, high flexibility, low weight, easily handle and broad-band acoustic performance (up to 10 MHz). The impacts were generated by dropping a 9 mm diameter steel ball on the surface of the plate in two different positions. Sensors location and impact source coordinates are reported in table 1.

Table 1 Sensors and impact coordinates in test 1.

	Sensor 1	***Sensor 2***	***Sensor 3***	***Sensor 4***	***Impact A 1***	***Impact A 2***
x-coordinate (mm)	100	420	420	100	207	270
y-coordinate (mm)	300	300	100	100	150	220

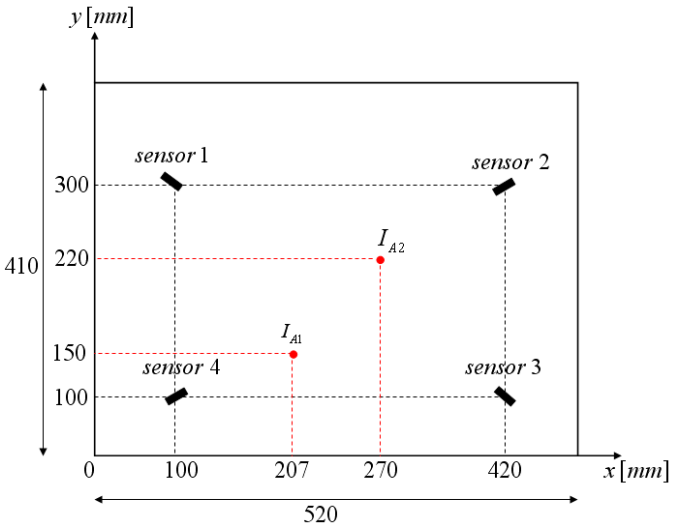

Figure 5 Experimental set-up and sensors arrangement in test 1

Test 2 consisted of an aluminium plate with dimensions 1487 mm x 999 mm x 0.98 mm instrumented with four 300 kHz Acoustic Emission sensors, provided by courtesy of Airbus UK (Fig. 9). The AE transducers were attached to the surface of the plate using non-corrosive coupling gel. They were firstly connected to pass-band filters with a frequency range between 200 and 400 kHz and then linked to preamplifiers. Two different configurations of the transducers location were studied, and the impacts were induced by a hand-held modal hammer, manufactured by Meggit-Endevco. Following tables show the sensors and impact coordinates in both configurations.

Table 2 Sensors and impact coordinates in test 2, configuration 1

	Sensor 1	***Sensor 2***	***Sensor 3***	***Sensor 4***	***Impact B 1***
x-coordinate (mm)	494	409	1156	1242	750
y-coordinate (mm)	332	723	778	167	500

Table 3 Sensors and impact coordinates in test 2, configuration 2

	Sensor 1	***Sensor 2***	***Sensor 3***	***Sensor 4***	***Impact B2***
x-coordinate (mm)	494	409	741	1156	890
y-coordinate (mm)	332	723	780	778	398

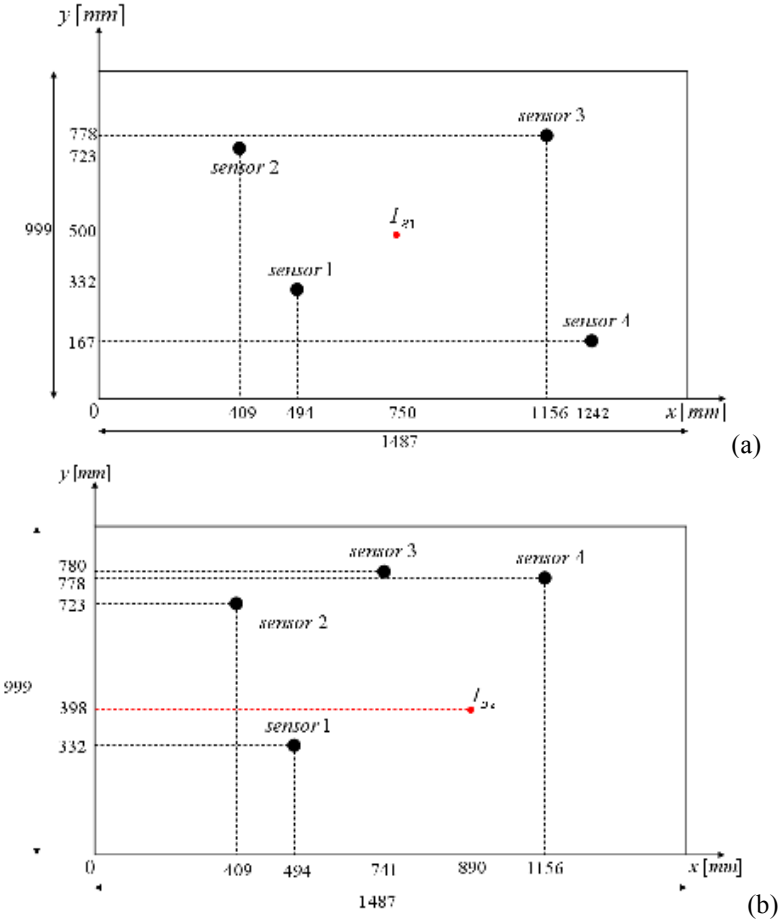

Figure 6 (a) (b) Experimental set-up and sensors arrangement in test 2.

For the signal acquisition, a four channel oscilloscope (Tektronic TDS 3014) with a sampling rate of 2 MHz was used, and it was triggered by one of the sensors (*master sensor*). The time histories of the signals received by the sensors were stored on a computer and processed using a Matlab software code implemented by the author.

6 Impact location results

The signals were analyzed in terms of group (energy) velocity–frequency relationship. A numerical routine was developed to find the A_0 Lamb wave mode peaks to extract the arrival time of the wave packets with largest energy contribution (ridges of the scalogram) (Fig. 7, 8, 9). Hence, according to Section 3, the maxima coefficients of the scalogram in both experiments were found at two different frequencies, 3452 Hz for the tests with the PVDF (referred as A1 and A2 in the article) and 273.4 kHz with

acoustic emission transducers (referred as B1 and B2 in the article). Therefore, arrival times of the flexural waves can be identified at these instantaneous frequencies. Nevertheless, it was noticed that the frequencies of interest 3452 Hz for the tests with PVDF (A1 and A2) and 273.4 kHz with acoustic emission transducers (B1 and B2) were not the same for all four sensors. This can be seen in sub-figure (c) of Figure 7, sub-figures (a) and (c) of Figure 8 and sub-figure (c) of Figure 9, wherein the time representation of the wavelet coefficients does not seem to match the maximum of contour plot of the relative scalogram. However, for those transducers for which the scalogram maximum coefficients resulted different, the associated frequency was approximately the same (a maximum difference of 10 Hz) with respect to the values mentioned above. This means that the arrival time evaluation error due to this frequency shift is negligible.

The results of the impact location and wave velocity identification are summarized in Fig. 7 for test 1 and are reported in Fig. 8 and 9 for test 2.

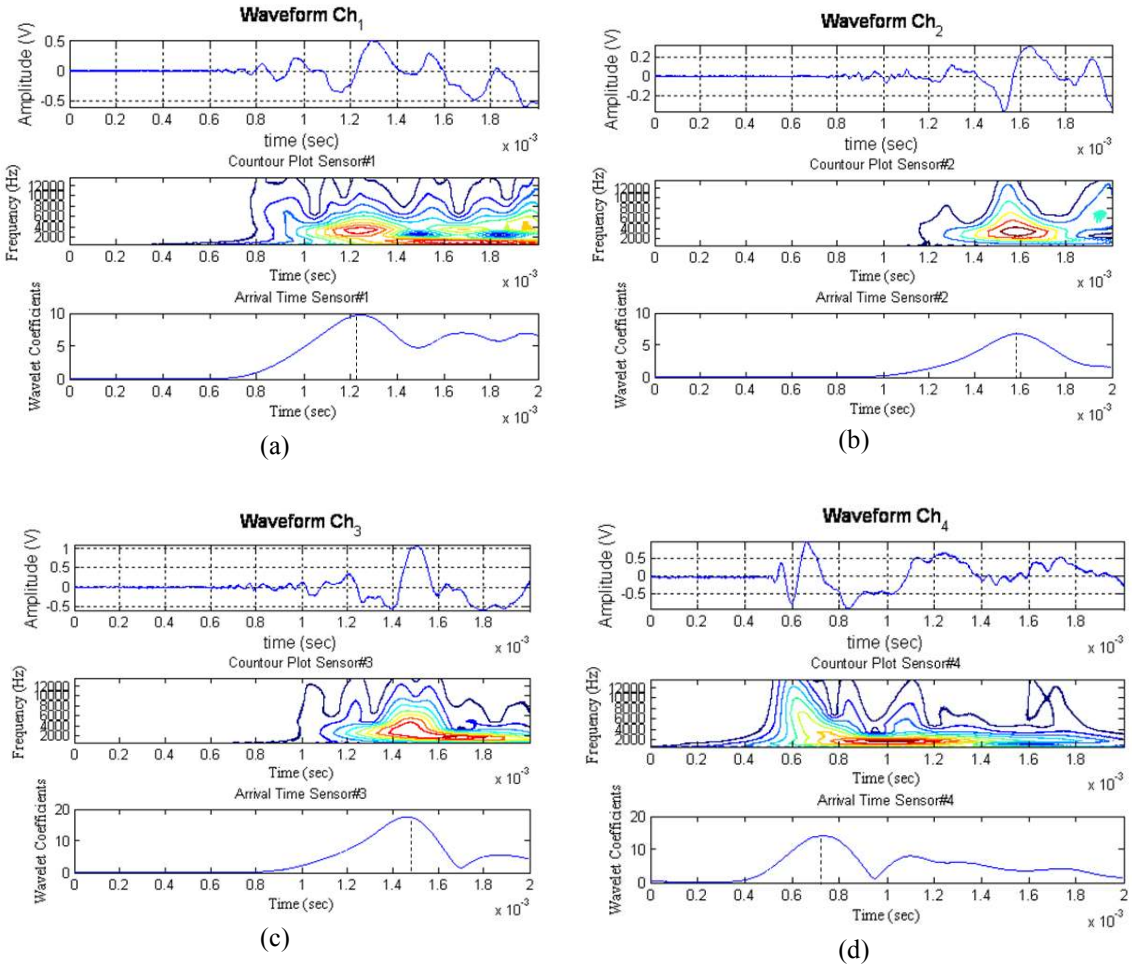

Figure 7 (a) (b) (c) (d) Each sub-figure illustrates the time histories of the four signals measured by the PVDF transducers, the contour-plot of the scalogram of the CWT and line profile of the scalogram illustrating the procedure to extract the TOA at $f = 3452\ Hz$ for test 1 and impact A1.

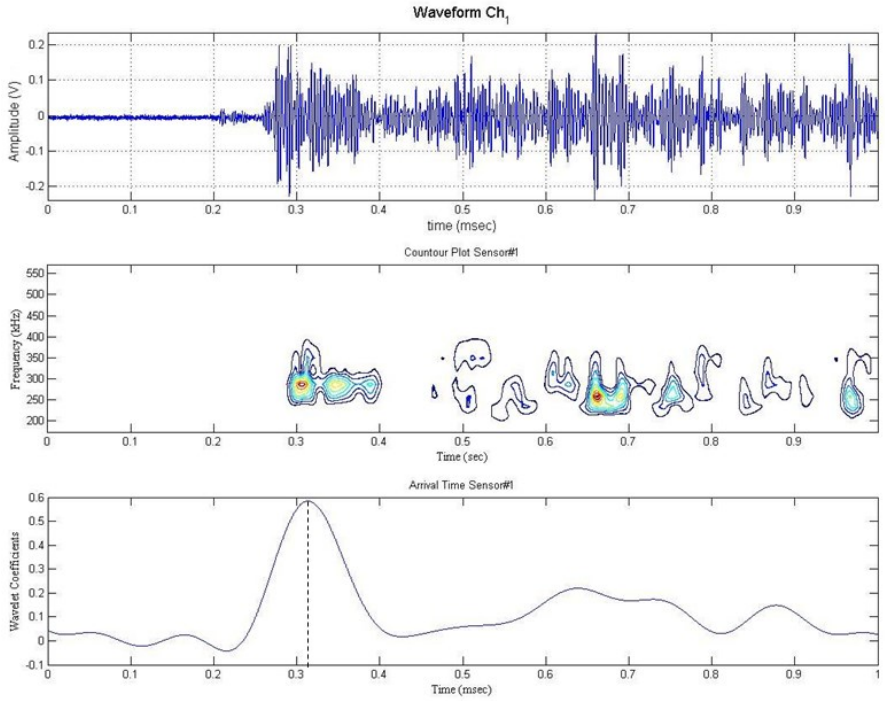
Waveform Ch1
Amplitude (V)
time (msec)
Countour Plot Sensor#1
Frequency (kHz)
Time (sec)
Arrival Time Sensor#1
Wavelet Coefficients
Time (msec)

(a)

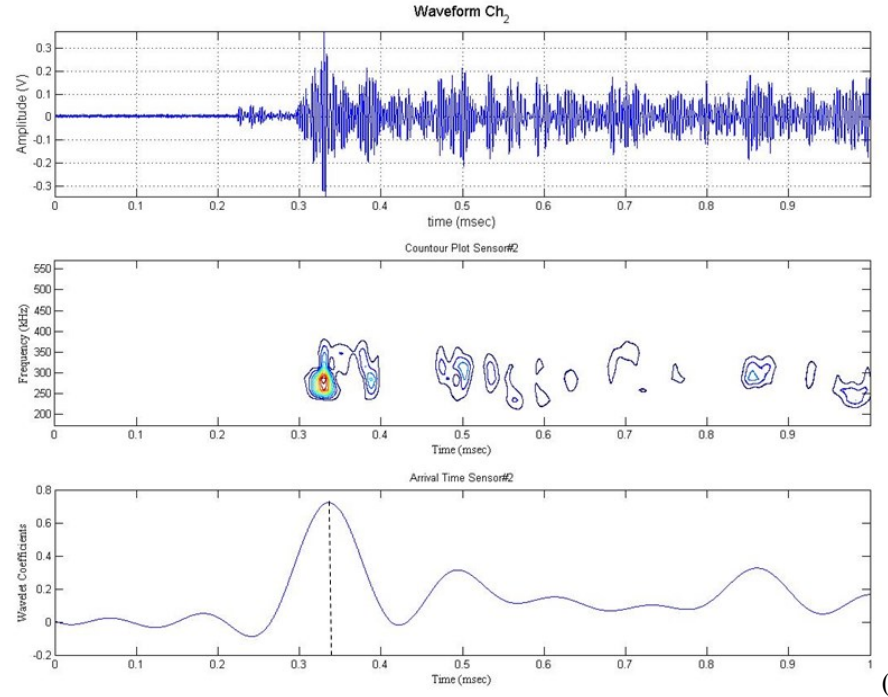
Waveform Ch2
Amplitude (V)
time (msec)
Countour Plot Sensor#2
Frequency (kHz)
Time (msec)
Arrival Time Sensor#2
Wavelet Coefficients
Time (msec)

(b)

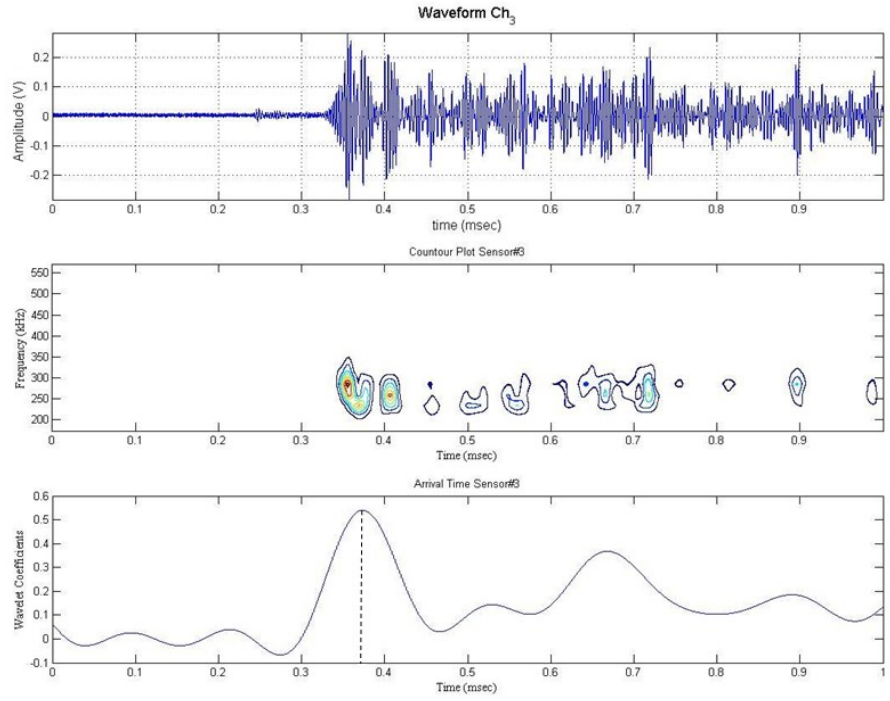

(c)

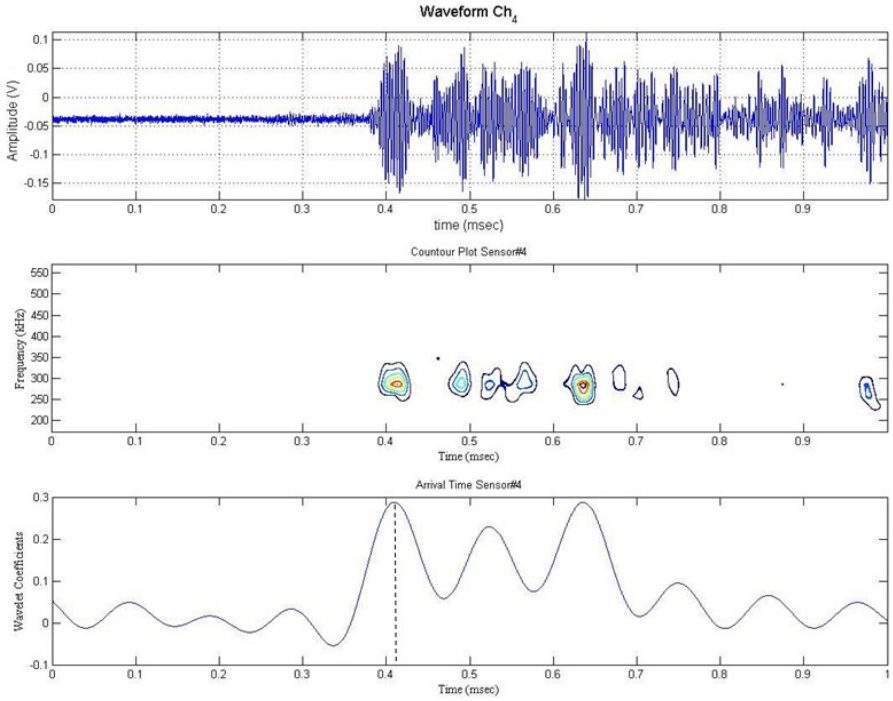

(d)

Figure 8 (a) (b) (c) (d) Each figure illustrates the time histories of the four signals measured by the acoustic emission transducers, the contour-plot of the scalogram of the CWT and line profile of the scalogram illustrating the procedure to extract the TOA at $f = 273.4\ kHz$ for test 2 and impact B1.

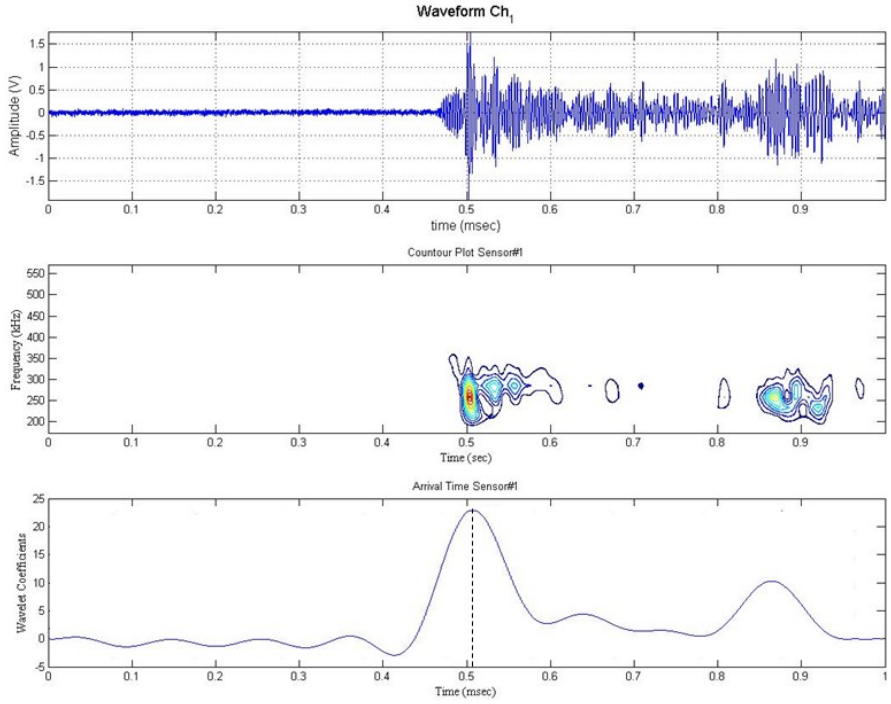
Waveform Ch1
Amplitude (V)
time (msec)
Countour Plot Sensor#1
Frequency (kHz)
Time (sec)
Arrival Time Sensor#1
Wavelet Coefficients
Time (msec)

(a)

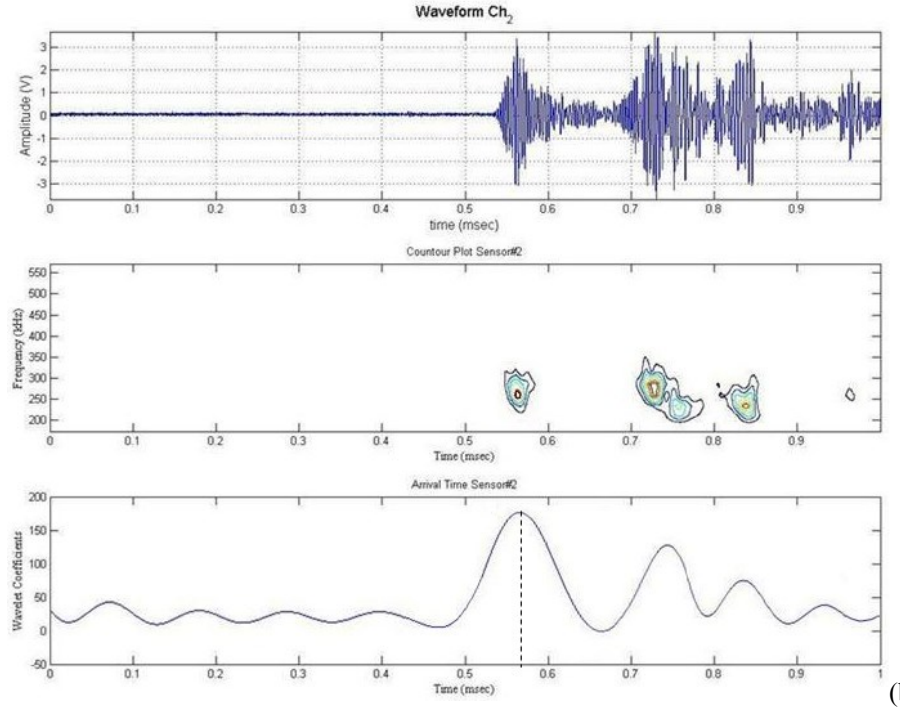
Waveform Ch2
Amplitude (V)
time (msec)
Countour Plot Sensor#2
Frequency (kHz)
Time (msec)
Arrival Time Sensor#2
Wavelet Coefficients
Time (msec)

(b)

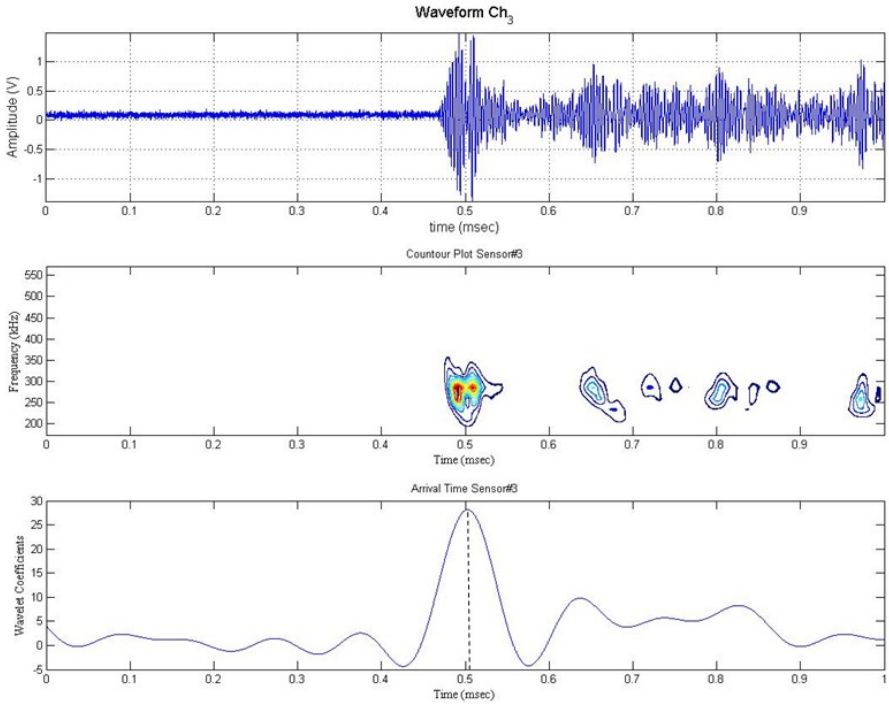

(c)

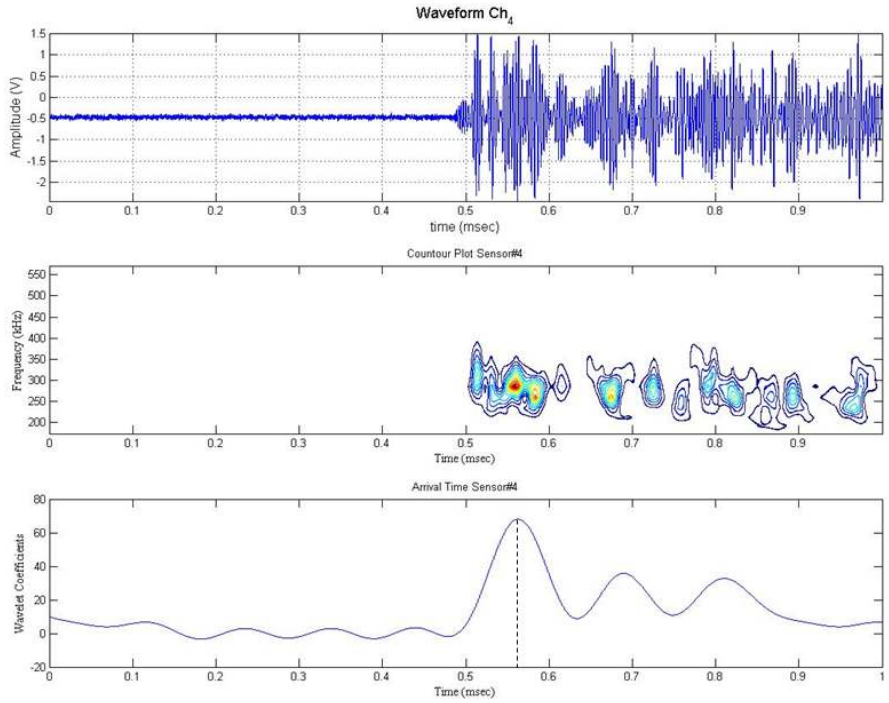

(d)

Figure 9 (a) (b) (c) (d) Each figure depicts the time histories of the four signals measured by the acoustic emission transducers, the contour-plot of the scalogram of the CWT and line profile of the scalogram illustrating the procedure to extract the TOA at $f = 273.4\ kHz$ for test 2 and impact B2.

The results of the predicted impact source location for both configurations in test 1 and 2 are shown in Fig. 10.

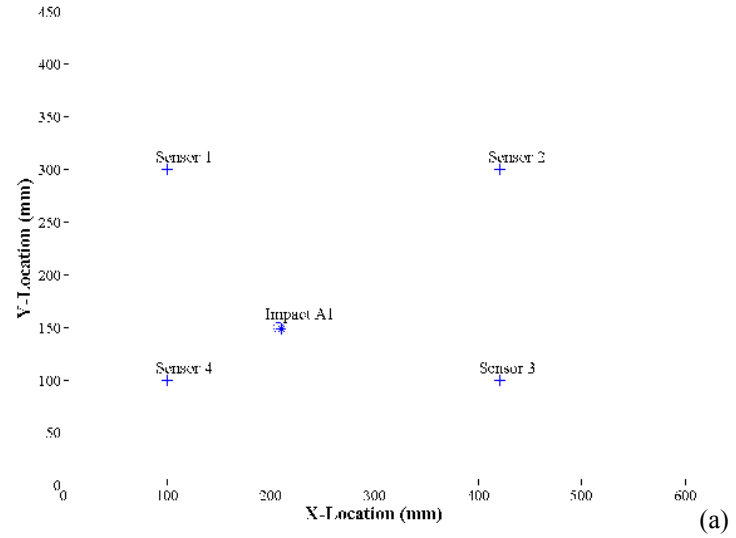
Sensor 1
Sensor 2
Impact A1
Sensor 4
Sensor 3
Y-Location (mm)
X-Location (mm)
0
50
100
150
200
250
300
350
400
450
0
100
200
300
400
500
600

(a)

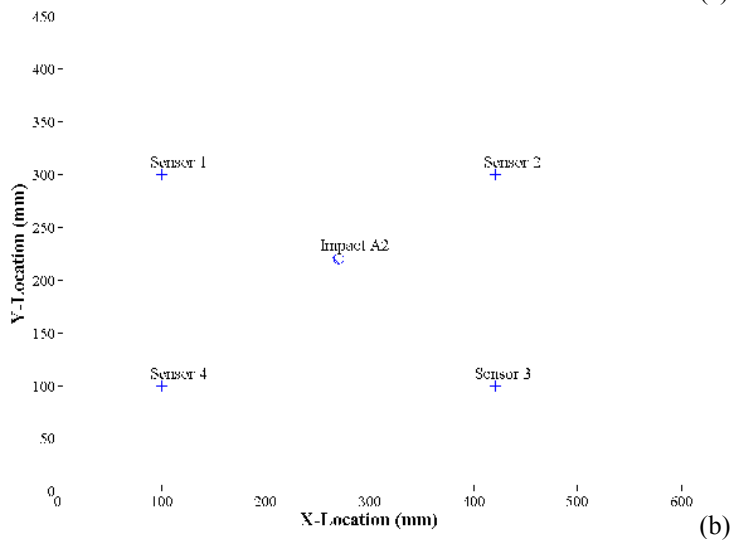
Sensor 1
Sensor 2
Impact A2
Sensor 4
Sensor 3
Y-Location (mm)
X-Location (mm)
0
50
100
150
200
250
300
350
400
450
0
100
200
300
400
500
600

(b)

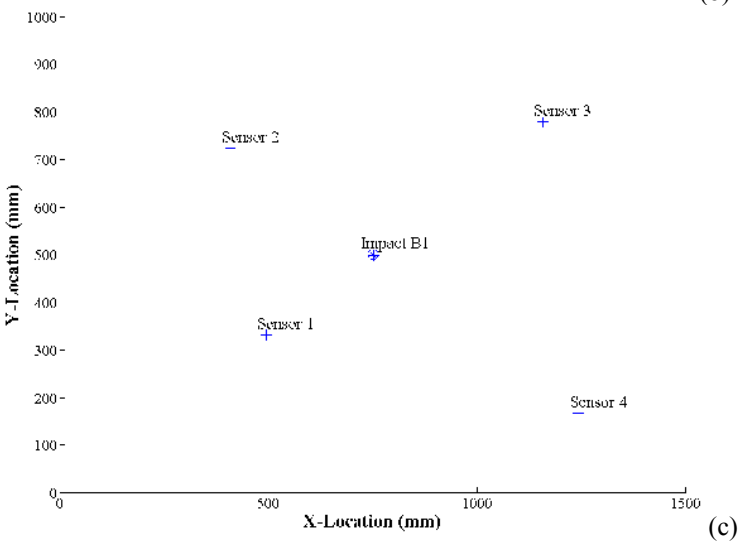
Sensor 3
Sensor 2
Impact B1
Sensor 1
Sensor 4
Y-Location (mm)
X-Location (mm)
0
100
200
300
400
500
600
700
800
900
1000
0
500
1000
1500

(c)

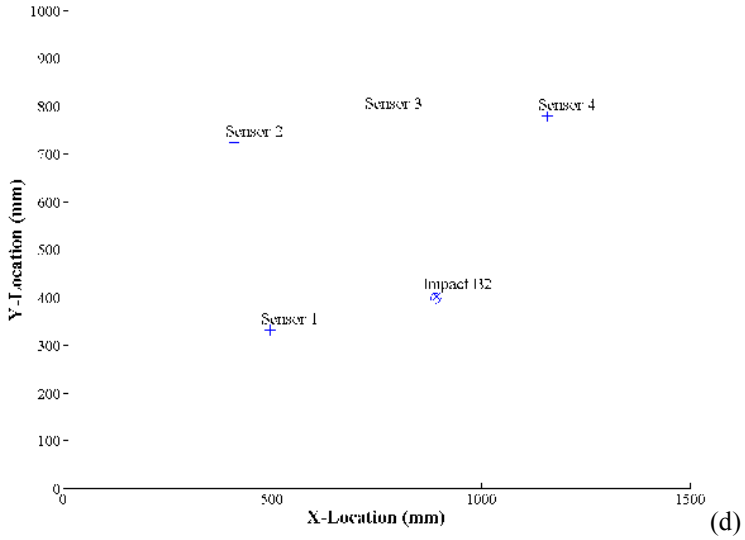

(d)

Figure 10 Source location results of test 1 (a) - (b) and test 2 (c) – (d). The calculated and true impact positions are shown as an open circle (o) and a star (*), respectively. The sensor positions are represented by a plus sign (+).

The following table reports the results of source location in terms of location error ψ defined in Paget's paper (2003).

Table 4 Impact positions and errors for test 1 and test 2

	Impact A1	**Impact A2**	**Impact B1**	**Impact B2**
x-coordinate source location (from algorithm)	209.8 mm	267.2 mm	752.23 mm	891.69 mm
x-coordinate source location (real value)	207 mm	270 mm	750 mm	890 mm
y-coordinate source location (from algorithm)	148.6 mm	218.4 mm	497.67 mm	401.42 mm
y-coordinate source location (real value)	150 mm	220 mm	500 mm	398 mm
Location error ψ	3.13 mm	3.22 mm	3.21 mm	3.63 mm

6.1 Group velocity evaluation

The velocity group values of A_0 Lamb wave mode of both aluminium specimens determined in the optimization procedure (see table 5), are compared with that obtained through an analytical approach using the Rayleigh-Lamb frequency relations (Viktorov, 1967) known as the dispersion equations. The wave numbers of antisymmetrical Lamb modes can be expressed as function of the frequency-thickness by the following equation (Fig. 11):

$$\frac{\tan\left(\frac{qd}{2}\right)}{\tan\left(\frac{pd}{2}\right)} + \frac{\left(q^2 - k^2\right)^2}{4k^2qp} = 0 \qquad (6.1)$$

where $q=\sqrt{k_t^2-k^2}$, $p=\sqrt{k_l^2-k^2}$, k is the wave number, $k_l^2=\left[\omega^2\rho/(\lambda+2\mu)\right]$, $k_t^2=\left(\omega^2\rho/\mu\right)$, λ and μ are the Lame constants, ρ is the density, ω is the angular frequency and *d* is the thickness of the plate. Relation analogous to (6.1) can be found for the group velocity by assuming $V_g=V_{ph}+k\dfrac{\partial V_{ph}}{\partial k}$ where V_{ph} is the phase velocity, expressed as $V_{ph}=\omega/k$.

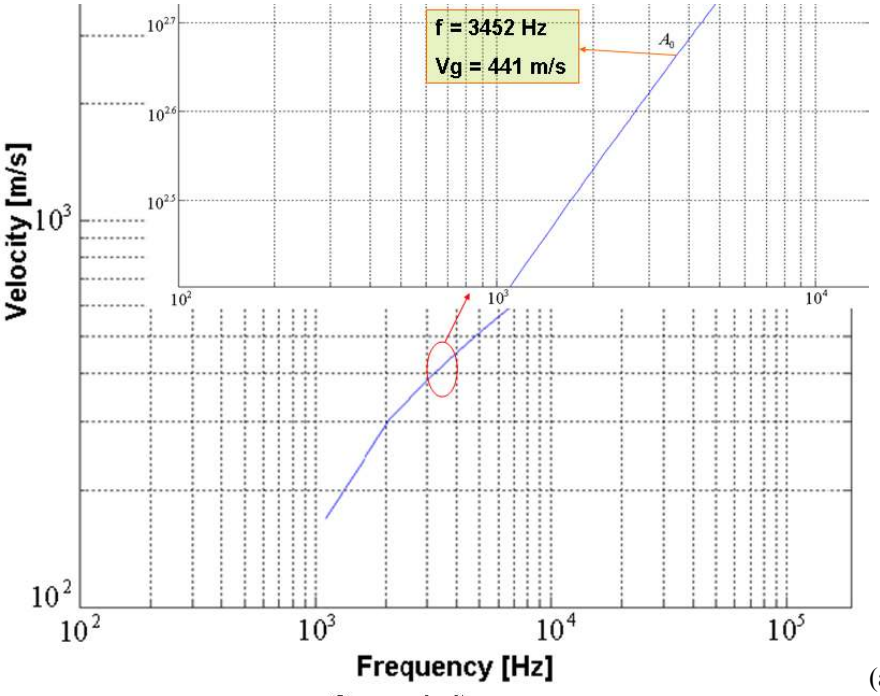

(a)

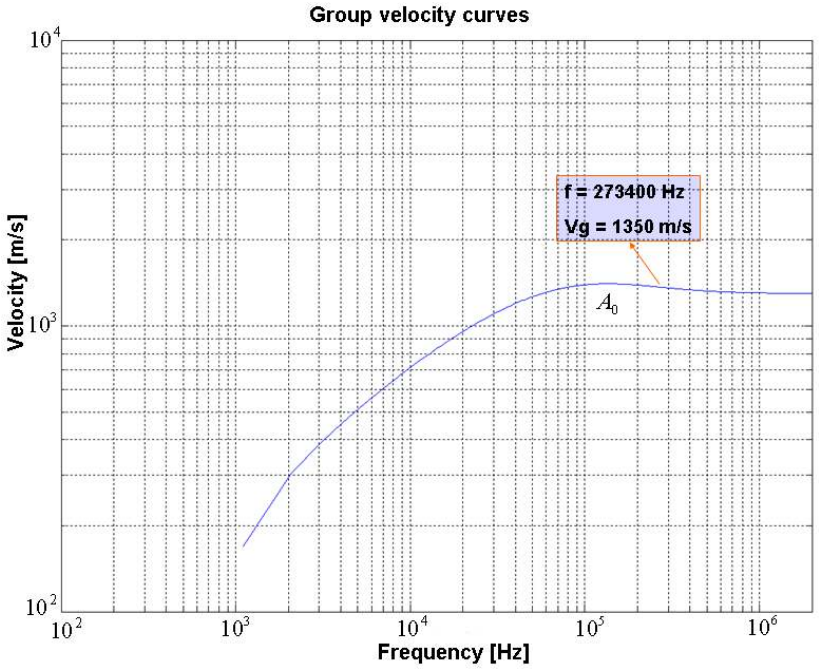

(b)

Figure 11 (a) (b) Dispersion curves of fundamental antisymmetrical Lamb mode for both aluminium plates. From test 1 (a), @ 3452 Hz the correspondent group velocity is at 441 m/s, whilst in test 2 (b), @ 273.4 kHz the correspondent group velocity is at 1350 m/s.

Table 5 Flexural Lamb mode wave velocity results for test 1 and test 2

	Impact A1	**Impact A2**	**Impact B1**	**Impact B2**
Group velocity (from algorithm)	439.4 m/s	442.6 m/s	1346.34 m/s	1353.05 m/s
Group velocity (from dispersion curves)	441 m/s	441 m/s	1350 m/s	1350 m/s

The general conclusions derived from the above table are that this algorithm generates results with reasonable accuracy (maximum error in estimation of the coordinates of the impact location was less than 4 mm and about 3 m/s for the wave velocity determination) for both types of impacts considered. In addition, from the experiments on the test 2, it was observed that whether the distance of the transducer from the impact source was bigger than 650 mm, the effects from the edges of the plate and the reflected waves led to a wrong estimation of the stress waves arrival time. Hence, an error of 27% on the impact source location was induced. This information can be useful for the optimal location of sensors bonded in large structures.

7 Conclusions

This research work presents an impact localization system able to identify the source of acoustic emission signals and to determine the velocity of flexural waves in isotropic structures. Four piezoelectric film and acoustic emission transducers were used to measure the Lamb modes. The relative signals were processed by the analysis of the Continuous Wavelet Transform (CWT). The information contained in the ridge of the scalogram of the CWT that represents the highest energy contribution of the signal, was employed to determine the time of arrival (TOA) of stress waves. The coordinates of the impact location and the wave velocity were calculated by solving a system of non linear equations by a combination of Line Search and backtracking techniques with a Newton's iterative method. One of the main advantages of the proposed algorithm is that it is able to converge from almost any guess point. Computational time for each source location to less than 2 s, meaning the impact algorithm can be obtained in quasi real-time using a compiled code.

This method overcomes the limits of a triangulation technique, as it does not require any knowledge of the material properties as well as a previous estimate of the group velocity. For the validation of the method, several experiments were carried out using two aluminium specimens. Good agreement between the theoretical and experimental results show that the point of impact and the wave velocity can be predicted with high accuracy. In particular, the maximum error in estimation of the impact location was less than 2% and about 1% for the flexural waves velocity.

Moreover, even if this study was based on measuring the flexural Lamb mode A_0, this method can be also applied to the inspection of the extensional Lamb mode.

References

[1] Balageas D, Fritzen C P, Güemes A. “Structural Health Monitoring”. ISTE LTD, 2006

[2] Brown L F. “Disposable PVDF ultrasonic transducers for non-destructive testing applications”. *IEEE Transaction on Ultrasonics, Ferroelectrics, and Frequency Control*, Vol. 43, No. 3, 2000, pp. 560-568

[3] Dennis J E, Schnabel R B. “Numerical methods for unconstrained optimization and non linear equations”. Soc. for Industrial & Applied Math., 1996

[4] El youbi F, Grondel S, Assaad J. “Signal processing for damage detection using two different array transducers”. *Ultrasonics **42***, 2004, pp.803-806

[5] Gaul L, Hurlebaus S, Jacobs L J. “Localization of a “synthetic” acoustic emission source on the surface of a fatigue specimen”. *Research in Nondestructive Evaluation*, 2001, pp. 105-117

[6] Gaul L, Hurlebaus S. “Determination of the impact force on a plate by piezoelectric film sensors”. *Archive of Applied Mechanics, **69***, 1999, pp. 691-701

[7] Giurgiutiu V. “Lamb wave generation with Piezoelectric Wafer Active Sensors for structural health monitorig”. *SPIE’s 10th Annual International Symposium on Smart Structures and Material and 8th Annual International Symposium on NDE for Health Monitoring and Diagnostics, San Diego, CA, 2002, paper # 5056-17*, pp. 1-12

[8] Haase M, Widjajakusuma J. “Damage identification based on ridges and maxima lines of the wavelet transform”. *International Journal of Engineering Science **41***, 2003, pp. 1423-144

[9] Hamstad M A. “On Use of Piezoelectric Polymers As Wideband Acoustic Emission Displacement Sensors for Composites". *Proceedings of Fifth International Symposium on Acoustic Emissions from Composite Materials (AECM-5), Sundsvall, Sweden, The American Society for Nondestructive Testing, Inc.*, 1995, pp. 111-119.

[10] Hamstad M A, O’Gallagher A, Gary J. “A wavelet transform applied to acoustic emission signals: Part 1: Source Identification”. *Journal of Acoustic Emission*, **20**, 2002, pp. 39-61

[11] Jeong H, Jang Y-S. “Fracture source location in thin plates using the wavelet transform of dispersive waves”. *IEEE Transaction on Ultrasonics, Ferroelectrics, and Frequency Control*, Vol. 47, No. 3, 2000, pp.612-619

[12] Kim H, Melhem H. “Damage detection of structures by wavelet analysis”. *Engineering Structures, **26***, 2004, pp. 347-362

[13] Kundu T, Das S, J K V. “Detection of the point of impact on a stiffened plate by the acoustic emission technique”. *Smart Materials and Structures **18***, 2009, pp. 1-9

[14] Kosel T, Grabec I, Kosel F. “Intelligent location of simultaneously active acoustic emission sources”. *Aircraft Engineering and Aerospace Technology*, Vol. 75, No. 1, 2003, pp. 11-17

[15] Le T-P, Argoul P. “Continuous wavelet transform for modal identification using free decay response”. *Journal of Sound and Vibration **277***, 2004, pp. 73-100

[16] Mallat S. “A wavelet tour of signal processing”. London: Academic Press, 1998

[17] Meo M, Zumpano G, Pigott M, Marengo G. “Impact identification on a sandwich plate from wave propagation responses”. *Composite Structures **71***, 2005, pp. 302-306

[18] Monkhouse R S C, Wilcox P W, Lowe M J S, Dalton R P, Cawley P. “The rapid monitoring of structures using interdigital Lamb wave transducers”. *Smart Materials and Structures **9***, 2000, pp. 753-780

[19] Nocedal J, Wright S J. “Numerical Optimization”. Springer Series in Operations Research, 1999

[20] Paget C A, Atherton K, O’Brien E. “Triangulation algorithm for damage location in aeronautical composite structures”. *Proceeding of the 4th International Workshop on Structural Health Monitoring, Stanford, CA*, 2003, pp. 363-370

[21] Reddy J N. “Theory and analysis of elastic plates”. Taylor & Francis LTD, 1999

[22] Seydel R, Chang F K. “Impact identification on stiffened composite panels: system development”. *Smart Materials and Structures **10***, 2001, pp. 354-369

[23] Sung D U, Oh J H, Kim C G, Hong C S. “Impact monitoring of smart composite laminates using neural network and wavelet analysis”. *Journal of Intelligent Material Systems*, Vol. 11, 2000, pp. 180-190

[24] Tobias A. “Acoustic emission source location in two dimensions by an array of three sensors”, *Non-Destructive Testing*, Vol. 9, No. 1, 1976, pp. 9-12

[25] Viktorov I A. “Rayleigh and Lamb waves. Physical theory and applications”. Plenum Press New York, 1967

[26] Ziola S M, Gorman M R. “Source location in thin plates using cross-correlation”. *The Journal of the Acoustic Society of America **90*** (5), 1991, pp. 2551-2556